ASME Journal of Engineering for Gas Turbines and Power
Online journal at:
https://asmedigitalcollection.asme.org/gasturbinespower

Effect of Film Cooling Hole Location on Flow Dynamics in a Rotating Detonation Combustor

S. Ramanagar Sridhara
Department of Industrial Engineering,
University of Florence,
Via S.Marta 3,
Florence 50139, Italy

Marc D. Polanka
Air Force Institute of Technology,
Wright-Patterson Air Force Base, OH 45433

Myles D. Bohon
Pressure Gain Combustion,
Technische Universität Berlin,
Berlin 10623, Germany

Antonio Andreini
Department of Industrial Engineering,
University of Florence,
Via S.Marta 3,
Florence 50139, Italy

Detonative combustion can be employed to develop high-power-density combustors, such as the rotating detonation combustor (RDC). The high combustor mass flow, combined with the significant heat release from detonation waves occurring near the walls of the narrow annulus, results in immense thermal loads on the walls. Managing these thermal loads is crucial for the successful application of RDCs in gas turbines. Previous studies have suggested that film cooling may offer a viable solution for mitigating the intense thermal loads. However, the impact of the coolant mass addition location on RDC performance remains unclear. Four film-cooled RDC architectures are investigated, where the holes covered different portions of the outer wall from near the reactant injection location to downstream in the oblique shock region. The high circumferential and axial pressure variations resulted in differing coolant flows, while the added coolant mass increased the chamber pressure. The increased chamber pressure significantly altered the fresh gas refill structure and the detonation height. Regarding cooling performance, the various cooling schemes had different impacts on how much the wall temperatures were reduced. Ultimately, having cooling further downstream was most effective at overall cooling of the outer wall. However, placing coolant jets in the detonation region modifies the initial mixture characteristics, affecting the detonation combustion. In each cooling scheme, the injected coolant reacted with the unburnt fuel, leading to additional secondary deflagration heat release, which reduced the amount of unburned hydrogen at the exit.
[DOI: 10.1115/1.4069476]

1 Introduction

Various types of rotating detonation combustors (RDCs) with different shapes [1] and sizes [2] have been studied by research groups worldwide. Among these, the annular RDC is considered the most suitable for gas turbine applications [3]. However, sustaining the detonation in a small annulus requires high mass flow rates, and the intense heat release near the walls, combined with complex shock wave interactions, leads to high wall thermal loads. Goto et al. [4] performed experimental analysis with an ethylene/oxygen rotating detonation engine. They reported higher heat flux values up to 5 MW/m^2. While Braun et al. [5] using computational fluid dynamics and method of characteristics with correlations reported 1 MW/m^2 for an RDC operating at one bar chamber pressure. These heat loads are an order of magnitude higher than what is observed in conventional GT combustors [5].

Managing these thermal loads is critical for the effective use of RDCs in gas turbine applications. While thermal barrier coatings may offer partial protection, they are expected to be insufficient for fully managing the thermal loads. Additionally, shock wave interactions may accelerate the wear of barrier materials. Film cooling, which creates a protective coolant layer to isolate the walls from hot gases, presents a promising solution for thermal load management in RDCs [6,7]. Previous investigations of a partially film cooled combustor revealed that even with shockwave disruption, the film was able to refresh itself after disruption from each wave passage [7].

Although film cooling is a well-established concept in the gas turbine community, it is a novel approach for RDCs, and only a few researchers have explored its application. Tian et al. [8] were the first to numerically investigate film cooling in an RDC. Using low-fidelity simulations of a micro-RDC with a single row of film cooling holes, they assessed the feasibility of the technique. Yu et al. [9] performed unsteady Reynolds-averaged Navier–Stokes simulations with single-step chemistry to study a similar micro-RDC with one row of film cooling holes. Their work focused on the effect of coolant mass flow on hole blockage caused by shock and detonation waves. They found that increasing the coolant mass flow reduced hole blockage and expanded the protective area of the coolant film. In subsequent work, Yu et al. [10] analyzed the influence of cat-ear-shaped film cooling holes on coolant spreading under various operating conditions. They concluded that cat-ear-shaped holes

Turbo Expo: Turbomachinery Technical Conference & Exposition (GT2025), June 16–20, 2025. GT2025.
Manuscript received July 7, 2025; final manuscript received July 22, 2025; published online September 24, 2025. Editor: Jerzy T. Sawicki.

provided superior cooling performance with reduced fluctuations in coolant mass flow. Most numerical studies in the literature, however, rely on low-fidelity simulations with premixed injection systems. Moreover, these studies, often limited to single rows of film cooling holes, report minimal or no influence of film cooling on detonation combustion.

The experimental studies by Chriss et al. [11] examined a six-inch film-cooled RDC with a film cooling configuration spanning the entire combustor. They investigated the effect of coolant mass flow on combustion dynamics, finding that higher coolant flow rates resulted in unstable operating modes, increased temperatures, and acoustic mode variations strongly influenced by coolant flow. However, their analysis did not address the impact of film cooling applied to specific regions of the combustor.

Yu et al. [12] conducted experimental studies on a hollow RDC with cat-ear-shaped film cooling holes, also applied across the entire combustor. They achieved a self-sustaining detonation wave with film cooling, observing that increased coolant mass flow raised chamber pressure and enhanced thrust. At lower coolant mass flows, wave velocities were comparable to the uncooled case, while higher flows increased wave speeds. Additionally, the coolant mass provided wall protection and improved overall performance.

Rotating Detonation Combustors, unlike conventional gas turbine combustors, are highly sensitive to physical boundary conditions such as combustor outlet restrictions [13], injector diameters influencing wave clocking [14], and various other factors. Film cooling is a novel concept for RDCs, where the introduction of coolant flow adds aerodynamic restrictions, creating a blockage effect similar to outlet restriction in the experimental investigations by Bach et al. [15]. However, the effect of mass addition on the combustion process remains an open question.

To explore the impact of coolant mass addition on overall combustor dynamics and its implications reducing the combustor wall temperatures, four film-cooled RDC configurations investigated using high-fidelity numerical simulations. This investigation is focused on studying the implications of adding coolant mass at different axial locations on the overall combustor dynamics. This includes the mixing in the detonation region, the overall impact on the detonation wave, and the heat release of the detonation combustor. Ultimately, the papers' goal is finding preferred locations for adding the coolant to cool the combustor hardware.

2 Film Cooling Configuration

The baseline uncooled RDC geometry was derived from the TU Berlin RDC architecture [14,16]. It features an annulus width of 7.6 mm, a mean combustor diameter of 9 cm, and a combustor length of 11 cm without outlet restriction. A chamber mass flux of 290 kg/sm^2, was chosen leading to air and fuel mass flow rates of 445 g/s and 13.3 g/s, respectively. This mass flux for an equivalence ratio of one in the experiments consistently results in a single wave operating mode [3]. Fuel was injected through 100 axial cylindrical injectors with a diameter of 0.5 mm, while air was supplied through a radial gas injector with a width of 1 mm as shown in the uncooled geometry of Fig. 1. This arrangement created a jet-in-crossflow configuration with a backward-facing step geometry. Fuel and air plenum pressures of 13.12 and 7.42 bar, respectively, were used to achieve the desired chamber mass flux.

The first film cooled configuration was taken from the previous work of Ramanagar et al. [7,17] where the cooling holes began at an axial location of 4 cm from the injector surface. This location represented the start of the oblique shock region. The film cooling configuration included holes with a diameter of 1 mm with an inclination of 30 deg arranged in a staggered configuration with pitch of four and six diameters in the circumferential and axial directions, respectively. As such each row of film coolant contained 60 holes. It was designated as "PC40" representing Partially Cooled combustor with holes starting from 40 mm. Figure 1 illustrates the layout for this and the other tested geometries.

In the second and third configurations, the cooling arrangement was moved into the detonation region. Two locations were selected based on the detonation height of the uncooled combustor. These configurations maintained the same cooling scheme as PC40, namely, eight rows of holes. For the second geometry, the first row of holes started at an axial location of 2.3 cm which corresponds to half of the uncooled detonation height. This setup was referred to as the Partially Cooled in the Detonation region (PC23). The third configuration extended the cooling further upstream, with the holes starting at 1 cm from the air injector plate and is labeled PC10.

The final configuration is an extension of PC40, where three additional rows were added upstream. Hence, the holes started from 2.2 cm and extended till 8 cm axial length, resulting in eleven rows of coolant holes. This provided full cooling coverage and was designated as the Fully Cooled combustor (FC22). From the previous studies by Ramanagar et al. [7], a coolant plenum pressure of 3 bar was chosen as a balance between avoiding hot gas ingestion into the coolant plenum while ensuring sufficient coolant flow. Therefore, a coolant plenum pressure of 3 bar, with air as the coolant, was used for all configurations investigated in this study.

2.1 Numerical Model. The large Eddy simulations (LES) were conducted using the AVBP code developed by CERFACS. AVBP is a Navier–Stokes, multispecies, fully compressible reactive solver [18]. It has been extensively validated for a wide range of flow configurations, including film cooling [18–21]. The current methodology, grid resolution, and solver setup are based on the prior work of Ramanagar et al. [7].

For temporal evolution, explicit time integration was performed with a dynamically enforced maximum CFL number of 0.7, resulting in a time-step of 6×10^{-9} s. The WALE LES model was employed in combination with the localized artificial diffusivity model to stabilize the numerical scheme. The hydrogen-air detonation was modeled using the 4S1R single-step reaction mechanism developed by Nassini et al. [22]. This reaction mechanism, which is compatible

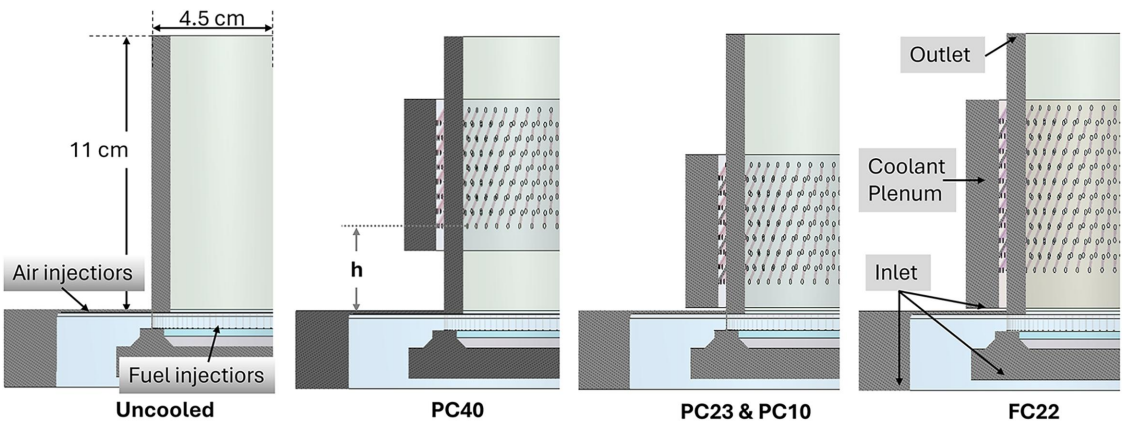

Fig. 1 Film cooled TU Berlin RDC geometry

with the Lax-Wendroff convection scheme, uses four species (H_2, O_2, H_2O, and N_2) in a single reaction. The solver setup, including time-step convergence and the reaction mechanisms used, was validated with the experiments by Nassini et al. [22], ensuring the robustness of the numerical approach for the current study.

The computational domain included the air, fuel, and coolant plenums, with all film cooling and injector holes, as shown in Fig. 1. Mesh sizes of 175 micrometers in the detonation region and 80 micrometers for injectors resulted in 380×10^6 elements for the partially cooled setup and 450×10^6 for the fully cooled configuration. The Celik quality index [23] ranged from 0.7 to 1.0, meeting the LES threshold of 0.8 or higher. Average y^+ values were 30–40 in the film cooling region and 20–80 in the detonation region, within the valid wall model range of 30–300. Pressure inlet and nonreflecting pressure outlet conditions were applied, while turbulent adiabatic wall functions in AVBP eliminated the need for prism layers. All these numerical schemes were previously used by Ramanagar et al. [7,17] to perform LES of film-cooled RDCs. The current film cooling simulations have not been validated experimentally, but they pave the way for the first experimental characterizations.

3 Results

3.1 Interaction of Chamber Pressure and Coolant Mass Addition. The detonation mode of combustion creates a significant variation in the combustor chamber pressure. The circumferential averaged pressure distribution across the axial length of the RDC obtained at 97% span is shown in Fig. 2(*a*). These profiles are obtained by circumferentially averaging the time-averaged 2D pressure distributions over 30 detonation wave cycles. The high-pressure detonation wave increases the average chamber pressure in the detonation region. Meanwhile, in the oblique shock region, the shock strength is lower than that of the detonation wave, resulting in a lower average chamber pressure. Specifically, for the uncooled RDC at 2 cm (detonation region) and 4 cm (oblique shock region) the circumferential average chamber pressure was 3.1 and 2.4 bar, respectively. This range of pressures partly drove the choice of 3 bar as the baseline coolant plenum pressure. Furthermore, significant circumferential pressure variation exists in the combustion chamber due to the presence of shock and detonation waves, as shown in the pressure profiles at 2.5 cm in Fig. 2(*b*).

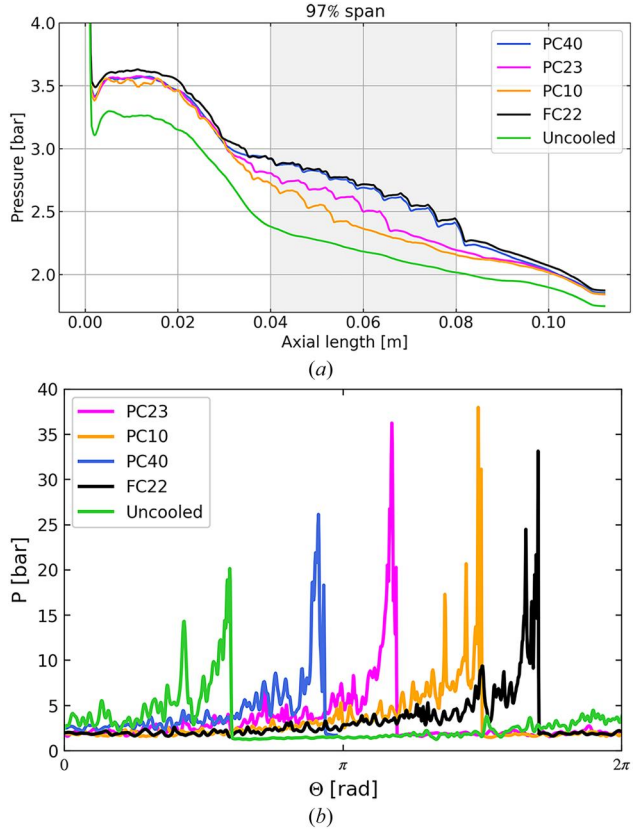

Fig. 2 (*a*) Circumferential average static pressure distribution across axial length and (*b*) instantaneous static pressure measurements obtained from pressure probe placed at 2.5 cm

This axial variation in circumferential averaged chamber pressure leads to corresponding variations in the coolant mass flow. For PC10, with holes starting at 1 cm, six of the coolant rows were located in the high chamber pressure region result in the lowest coolant mass flow of 54 g/s. In PC23, with holes starting at 2.3 cm, resulting in three coolant rows in the detonation region and the rest in the lower chamber pressure region, increases the coolant flow to 64 g/s. While PC40, with the holes starting aft of the detonation at 4 cm, achieves 71 g/s. The fully cooled configuration, with rows starting at 2.2 cm created a coolant mass flow of 81 g/s caused by the inclusion of three additional rows of holes.

The added coolant mass, due to the small combustor volume, elevates the overall chamber pressure (Fig. 2(*a*)) and raises the local minimum pressure in the detonation region. For the uncooled combustor, the local minimum pressure was 1.3 bar, increasing to 1.45, 1.6, and 1.75 bar for PC10, PC23, and PC40, respectively. The FC22 configuration further elevates the local minimum pressure to 1.9 bar, all with corresponding increases in the circumferentially averaged pressures as shown in Fig. 2(*a*). Interestingly, these variations in chamber pressure modify the detonation wave height and its three-dimensional structure. By analyzing the average heat release profiles at 3% span, as previously accomplished by Ramanagar et al. [17], the detonation wave height was determined to be 4 cm for PC10 and 3.5 cm for PC23 and PC40. FC22 had a height of 3.1 cm due to the highest chamber pressure.

Likewise, an increase in the chamber pressure altered the detonation wave in each case as seen in Fig. 2(*b*). In this figure, the instantaneous pressure traces obtained at the last wave cycle are adjusted by modifying their time for better visibility. The uncooled case exhibited a peak pressure of 20 bar and a secondary peak of 15 bar, caused by radial pressure reflections of the detonation wave, as noted by Zhao et al. [24]. For PC40 the peak detonation pressure was elevated to 25 bar while eliminating secondary reflections, indicating significant changes in the detonation wave's height and structure. In the PC23 and PC10 cases, where coolant was introduced in the detonation region, even higher peak detonation pressures were observed. This resulted from increased mixture density due to the addition of cold coolant gases, which strengthens the detonation wave, as discussed further in the upcoming sections. Furthermore, the comparative variations in chamber pressure across all cases are minimal, resulting in an insignificant variation in wave speed. The wave speeds were computed by performing Fourier transforms on the pressure profiles of 30 detonation wave revolutions resulting in an average variation between the various cooling configurations of 10–20 m/s.

3.2 Transient Response in the Film Cooling Holes. The mass flow through each hole is driven by the pressure difference across it. For a fixed coolant plenum pressure, variations in chamber pressure create nonuniform pressure ratios at different circumferential positions, resulting in uneven coolant mass flow. Figure 3 shows the phase-averaged coolant mass flux, coolant temperature, and water content (H_2O mass flux) for each hole at three axial locations: 27 mm, 51 mm, and 74 mm, representing high, medium, and low chamber pressure regions. These values were calculated on a cut plane located at one-third of the hole height (near the combustor), a method validated by Ramanagar et al. [17], to effectively capture hole-specific mass flow responses. Each dot represents the mean quantity for a hole, with vertical error bars indicating statistical variance. The results are plotted relative to the detonation wave, where the x-axis represents the detonation position. Positive x-values correspond to regions ahead of the detonation in the laboratory frame of reference, while negative x-values represent

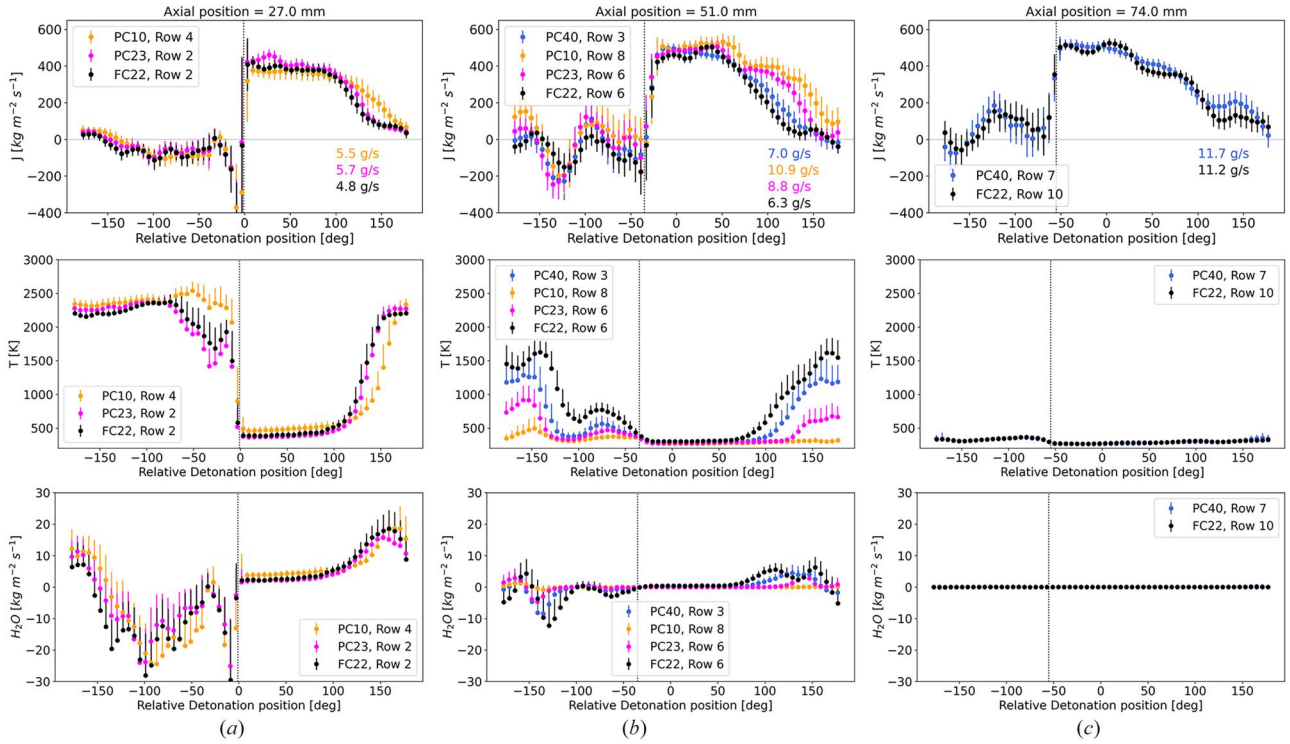

Fig. 3 Phase-averaged flow quantities for each hole, the top row illustrates coolant mass flux, the middle row shows gas temperatures inside the hole, and the bottom row presents water mass flux, measured at positions 27 mm (*a*), 51 mm (*b*), and 74 mm (*c*)

regions behind the detonation or shock wave, where chamber pressures are higher. The vertical dotted line represents the location of the shock wave at the given axial location.

The plots in Fig. 3 can be divided into three regions. The first is the blocked region, where negative mass flux occurs due to chamber pressures exceeding the coolant plenum pressure, located behind the detonation or shock wave. The second is the recovery region, where blocked coolant flow transitions to maximum flow. The third is the maximum flow region, characterized by high coolant mass flow occurring due to low chamber pressure, found ahead of the shock wave. The circumferential widths of these regions vary across axial locations due to significant differences in local chamber pressures.

In the high-pressure detonation region at 27 mm, the blocked region spans from 0 deg to −150 deg, where reverse flow causes hot combusted products (around 2500 K and 20 kg/m^2s water mass flow) to enter the coolant holes and penetrate into the plenum, as seen in the gas temperature and water mass flux plots in Fig. 3. This is most evident for the PC10 case since the first four holes are in the detonation region, more hot products accumulate inside the coolant plenum, leading to an increase in coolant temperature. During the recovery phase (−150 deg–100 deg), these hot gases are expelled back into the combustor annulus, with transient mass flux observed in the hole due to chamber pressure variation. Again, the PC10 case reflects the highest recirculated of products back into the fresh gas regions in this region.

In the maximum flow region (0 deg–100 deg), effective coolant delivery is achieved, with a mass flux of 400 kg/m^2s at temperatures of 300 K. These circumferential transients result in coolant mass flows of 5.5, 5.7, and 4.8 g/s for the cases flowing coolant at this location, namely, the PC10, PC23, and FC22 cases, respectively. The variations are due to differences in hole locations, as the cut plane represents the second hole for PC23 and FC22 while this is the 4th row for PC10. Moreover, these cases had different detonation heights and thus detonation strengths leading to different pressure profiles.

In the midcombustor region at 51 mm, the reduced chamber pressure delivers higher mass flow from the coolant plenum. The maximum mass flux increased to 500 kg/m^2s. Furthermore, the width of the maximum flow region with low temperature coolant increases substantially from roughly 80 deg to over 110 deg (−30 deg–80 deg). Subsequently, the blocked region shrinks to the circumferential angles from −180 deg to −40 deg, where flow alternates between reverse and positive directions. This results in reduced hot gas ingestion into the coolant plenum, as indicated by the water mass flux, which peaks at 10 kg/m^2s.

The recovery region broadens compared to detonation region profiles and contains fewer combusted products. The transient mass flow yields average coolant flows of 10.9, 8.8, 7.0, and 6.3 g/s for the PC10, PC23, PC40, and FC22 cases, respectively. These differences arise partly from chamber pressure variations. But they are also influenced by the pressure balancing within the coolant plenum. For the PC10 case, this axial location corresponds to the last row of holes, creating a preference for coolant to exit at this more downstream location rather than at upstream locations in the detonation region. This higher flowrate results in colder temperatures exiting the PC10 hole at this location.

Toward the end of the film cooling region at 74 mm, where chamber pressures are lower than upstream regions, the blocked region completely disappears. There is no ingestion of hot gases as shown in the gas temperatures and water mass flow plots. The maximum mass flow remains near 500 kg/m^2s ahead of the oblique shock wave. Due to the high mass flux in the recovery region, the integrated mass flows are 11.7 g/s for PC40 and 11.2 g/s for FC22. The slightly lower mass flow for FC22 is due to a higher chamber pressure. These higher flow rates out these downstream holes again is attributed to the preference of the coolant to exit here instead of further upstream.

3.3 Effect of Mass Addition on the Temperature Fields. The purpose of film cooling is to create a cold gas barrier that protects the walls from hot combustion gases. In the RDC, circumferential variations in coolant flow result in differing coolant jet momentum fluxes. Ahead of the shock wave, where coolant mass flow is higher, the coolant jet penetrates up to 75% of the span in the detonation

region and 50% at the last row [17,25]. While this penetration reduces gas temperatures, reactions between unburnt hydrogen and the coolant cause localized temperature increases. To evaluate these effects at various axial locations, gas temperatures between film cooling rows are averaged. Each region spans from the exit of one hole to the start of the next row, with a width matching the tangential pitch. The phase-averaged gas temperature at 97% span are presented in Fig. 4. The averages are performed for 30 detonation laps.

To understand the impact of the cooling holes, the uncooled case serve as baseline for comparison. In the detonation region at 27 mm, peak temperatures, around 3000 K, are observed behind the detonation across all cases, particularly within the blocked region where no coolant flow occurs, making all cases similar to the baseline. In the recovery region (100 deg–180 deg), the injection of ingested burnt gases back into the combustor increases temperatures, with film-cooled cases showing higher values than the uncooled case. In the maximum mass flow region (0 deg–100 deg), the PC40 case (which has not injected any coolant flow at this location) shows a temperature increase compared to the uncooled case due to flow field modifications from pressurization. Conversely, all other film-cooled cases exhibit a temperature decrease, most notably in the PC10 case, which injects coolant further upstream. This configuration achieves a 500 K reduction in minimum gas temperature, though this benefit lasts for less than a quarter of the cycle.

In the midcombustor region at 51 mm, within the blocked region (−180 deg to −40 deg), oscillations in coolant mass flow create wavy temperature profiles. Small dips in gas temperature are observed at −100 deg and −150 deg, where initial recoveries occur. The initial recovery and blockage stems from chamber pressure variations caused by reflected pressure waves from the high-pressure detonation wave. These reflections, traveling with the detonation wave, induce mass flux variations at the same frequency.

Ahead of the shock wave, where coolant flow is highest, the PC23 and PC10 cases show a significant reduction in gas temperature. At this axial location, PC10 has its 8th row and PC23 its 6th row of cooling holes. The higher cumulative coolant flow in these cases results in greater temperature reduction, with PC10 having 2 g/s more coolant flow than PC23 and achieving temperatures 100 K lower. Of note is that the FC22 case tracks the PC40 profile more than the PC23 profile. This is attributed to less coolant being ejected at the earlier hole locations for FC22 as it can preferentially send more of its mass flow further downstream.

At the end of the film cooling region, at 74 mm, the coolant always exits the holes, without hot gas recirculation, resulting in significant temperature decreases. Compared to the uncooled case, both PC40 and FC22 exhibit reductions across all regions, with the most pronounced cooling observed between −120 deg and 100 deg. Temperatures for the cooled cases drop below 2200 K, representing a reduction of 500 K compared to the uncooled case. While the injected coolant retains cooling potential, its impact starts to diminish further downstream as it mixes with the hot gases. This phenomenon can be observed in the PC10 and PC23 cases where the coolant flow ended upstream of this location. In the PC10 case, where mass addition stopped at 51 mm, the temperature is quickly approaching the uncooled wall temperature again. Similarly, for the PC23 case, while still relatively cold temperatures exist at this location, the minimum wall temperature has already increased by more than 300 K. At 97% span, the overall average gas temperature is 2000 K for the uncooled case. Film cooling reduces this to 1923 K for PC10, 1890 K for PC23, 1858 K for PC40, and 1851 K for FC22. Similar temperatures are observed for cases with mass addition starting from 20 cm. However, for PC10, the absence of mass addition beyond 51 mm causes the average gas temperature to approach that of the uncooled case.

3.4 Influence of Mass Addition on the Fresh Gas Mixing. To evaluate the impact of coolant mass addition on fresh gas mixing, several cut planes were created in the refill region. Time-averaged data of gas temperature, hydrogen mass fraction, and heat release were extracted from a plane located 10 deg ahead of the detonation wave. The time averages were performed for twenty detonation passages. This approach provides insights into the gas composition consumed by the detonation wave and the fluid properties through which it propagates. In the contours shown in Fig. 5, the light blue

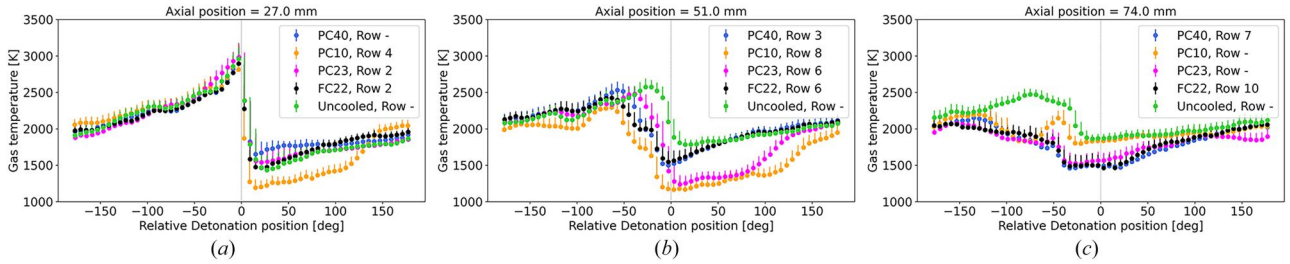

Fig. 4 The phase-averaged gas temperature obtained in the region ahead of each hole at 97% span at (*a*) 27 mm, (*b*) 51 mm, and (*c*) 74 mm

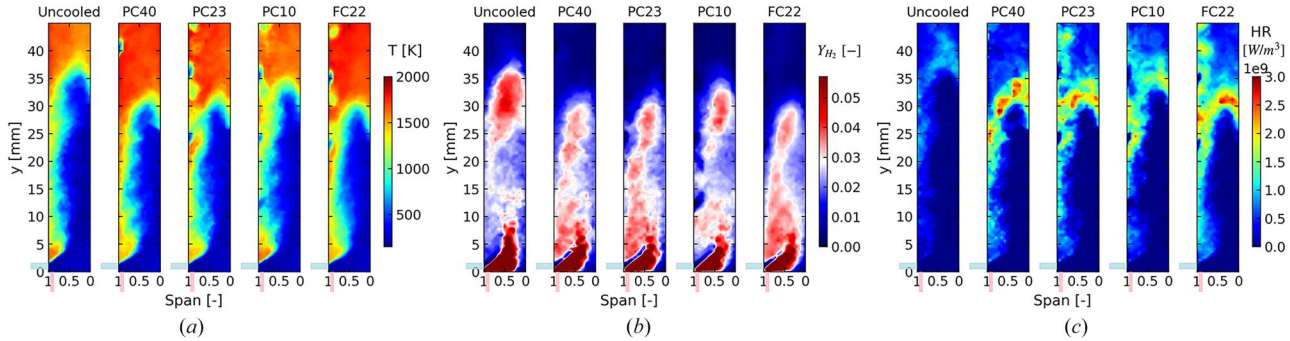

Fig. 5 Comparison of cut planes obtained at 10 deg ahead of the detonation wave for the various cooling schemes: (*a*) temperature, (*b*) hydrogen mass fraction, and (*c*) heat release

patch at an axial location of zero indicates the radial air injection point, while the pink patch at a span of one corresponds to the axial hydrogen injection. The radial dimension spans from zero (inner diameter) to one (outer diameter), representing the nondimensionalized span.

The shape of the fresh gas region, visualized using temperature contours in Fig. 5(*a*), reveals key characteristics of mixing. Gases with temperatures above 1500 K represent burnt products, while those between 700 and 1200 K indicate dilution zones, where parasitic burning occurs due to the interaction between fresh and burnt gases. The reactants are represented by the temperatures below 500 K. In the uncooled case, the fresh gas region extends up to 35 mm, with a recirculation zone forming at 5 mm. In the PC40 case, with coolant mass addition starting from 40 mm, the chamber pressure rises to 1.75 bar, compressing the fresh gas region to a height of 30 mm and widening the recirculation zone.

For PC23 and PC10, the chamber pressures decrease to 1.6 and 1.45 bar, slightly increasing the refill height and altering the recirculation characteristics. In these cases, coolant flow (with holes starting at 23 mm and 10 mm, respectively) reshapes the refill region at the point of injection. The FC22 configuration, despite its higher chamber pressure of 1.9 bar, exhibits a refill region and recirculation pattern similar to the PC23 case, highlighting the influence of hole placement and coolant interaction.

The hydrogen mass fraction contours in Fig. 5(*b*) reveal the distribution of fresh gas compositions. White regions represent stoichiometric mixtures, while blue and red indicate lean and rich zones, respectively. In the uncooled case, rich regions are concentrated near the injectors at the bottom, with a stoichiometric zone extending from 10 to 25 mm. At 30 mm, a rich buffer region forms, surrounded by a thin stoichiometric layer. This buffer arises from rapid recovery of the hydrogen injectors following blockage caused by the high-pressure detonation wave, as described by Nassini et al. [22]. The buffer region is not consumed by the detonation combustion leading to a presence of unburnt hydrogen in the postdetonated products. Additionally, lean mixtures are observed in the recirculation region between 1 and 5 mm.

In the PC40 case, increased chamber pressure alters the injector response, redistributing the rich buffer region into the midspan zone, surrounded by stoichiometric mixtures. Rich mixtures also accumulate in the recirculation region due to cross-jet momentum changes. In the PC23 case, coolant injection at 23 mm modifies the distributions in the region between 20 and 25 mm. In the PC10 configuration, where coolant holes are positioned further upstream, the chamber pressure is relatively close to that of the uncooled case, with only a 0.15 bar increase. As a result, the overall refill region shape remains closer to the uncooled configuration. However, significant differences are observed in the distribution of hydrogen mass fraction. Notably, within the region below 10 mm, there are larger stoichiometric zones compared to other film-cooled cases. This is attributed to the coolant jets penetrating into the fresh gases, which enhances dilution. Additionally, the size of the rich buffer region is reduced compared to the uncooled case, highlighting the impact of upstream coolant injection on mixture composition.

The FC22 configuration, characterized by high chamber pressure, exhibits similar distribution patterns to PC40. However, because coolant injection begins upstream at 22 mm, the mixture distributions closely resemble those of PC23. Overall, the presence of coolant significantly alters the mixture distributions by influencing chamber pressure and jet penetration. These effects highlight how film cooling affects the flow and combustion dynamics, especially in reshaping the rich and stoichiometric zones critical to combustion efficiency and detonation wave propagation.

Parasitic burning in each configuration is analyzed using heat release contours scaled to deflagration levels (Fig. 5(*c*)). In the uncooled case, mild parasitic combustion occurs at the interface of fresh and burnt gases, as evidenced by stoichiometric mixture regions in the hydrogen distribution contours. These interactions result in localized heat release at the contact points. In the PC40 case, increased chamber pressure and altered gas distributions within the refill region enhance the strength of parasitic heat release. The redistribution of rich and stoichiometric mixtures results in a broader heat release region compared to the uncooled case.

The PC23 configuration exhibits similar heat release levels to PC40 but introduces unique effects due to coolant injection at 23 mm. Here, the coolant reacts with unburnt hydrogen in the burnt products, leading to additional heat release near the outer wall above 30 mm. In PC10, lower chamber pressure and enhanced dilution from upstream coolant jets reduce deflagration levels. Moreover, the temperature of the injected coolant was higher with more burnt gas concentration, as discussed in Sec. 3.3. The penetration of these gases into the fresh gas modifies the distribution, resulting in diminished heat release near the wall. Conversely, the FC22 case, characterized by high chamber pressure, mirrors PC40's deflagration levels but shows concentrated heat release near the outer wall, a pattern driven by the interaction of coolant jets with gas distributions.

The distribution of fresh gases is highly dependent on chamber pressure. The height of the fresh gas region dictates the shape and height of the detonation wave, which, in turn, influences overall chamber pressure variations. The impact of coolant mass addition on the detonation wave is evident in the phase-averaged temperature distributions shown in Fig. 6. As observed, the shape of high-pressure regions differs in the film-cooled cases. At an axial position of 5 cm, oblique shocks in the cooled cases lag behind those in the uncooled case due to the reduced detonation height and variations in its shape.

Additionally, the lower gas temperature caused by coolant injection reduces the speed of sound, leading to faster-moving shocks near the outer wall. With the same detonation speed and oblique shock angle but a reduced detonation height, the phase shift between the detonation and oblique shock positions at a given axial location increases due to geometric effects. This accounts for the discrepancy in uncooled shock positions at 51 mm and 74 mm in Fig. 4.

Placing coolant holes in the detonation region promotes burnt gas recirculation; however, the burnt gas composition is lower due to the increased coolant volume in the plenum. Additionally, injecting coolant closer to the injectors can help mitigate rich-zone formation.

3.5 Heat Release Distributions. The increase in chamber pressure enhances the overall heat release of the combustor. Additionally, unburnt hydrogen from detonation combustion reacts with oxygen in the coolant, resulting in secondary heat release. This

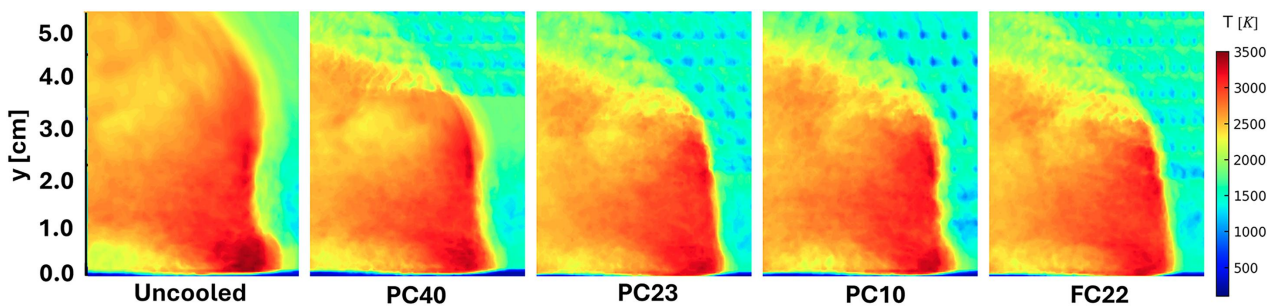

Fig. 6 Phase-averaged temperature distributions of the detonation wave obtained closer to the outer wall

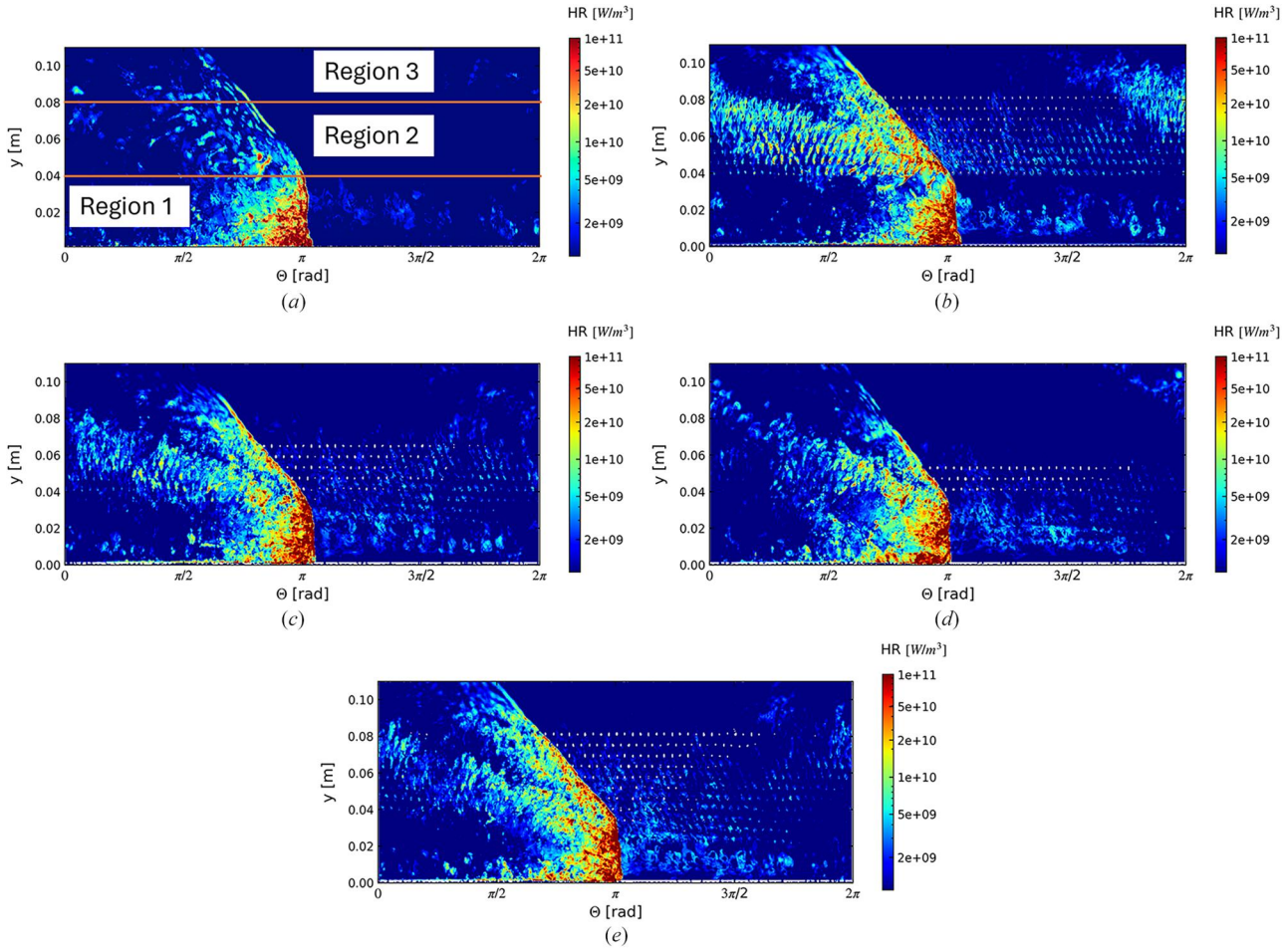

Fig. 7 Heat release contour obtained on a cut plane closer to the outer wall for (*a*) uncooled, (*b*) PC40, (*c*) PC23, (*d*) PC10, and (*e*) FC22 case

secondary combustion is visualized through heat release contours on the outer wall, as shown in Fig. 7. To quantify the heat release effects, the combustor is divided into three regions: Region 1 spans from the inlet to 4 cm, Region 2 extends from 4 cm to 8 cm, and Region 3 covers the area from 8 cm to the outlet. The volume-averaged heat release for these regions is reported in Table 1. These values are obtained by averaging 13 samples of volume-averaged data.

The uncooled case exhibits typical behavior: maximum heat release occurs at the detonation front, with deflagration combustion of unburned hydrogen behind the detonation wave. Additionally, a lower heat release is observed behind the oblique shock, where high pressure enhances reactivity. The heat release in Region 1 is 16,519 MW/m^3, while Regions 2 and 3 show lower values.

In the PC40 configuration, increased chamber pressure in the refill region leads to stronger deflagration heat release, and the detonation strength surpasses that of the uncooled case, resulting in higher heat release in Region 1 (25,886 MW/m^3). As shown in Fig. 7(*b*), heat release increases starting at 4 cm, coinciding with coolant mass addition. This increase in heat release, both behind and ahead of the shockwave, is due to the reaction of unburned hydrogen with oxygen in the coolant. Two distinct streams of maximum deflagration heat release are observed: one immediately following the shockwave and the other at a lower angle. These streams track the remnants of the coolant exiting the hole prior to the wave coming by and then the reemergence of the coolant after the pressure wave passes. Enhanced heat release in Regions 2 and 3 leads to a higher average heat release, almost four times the uncooled case. Additionally, unburned hydrogen consumption improves combustion efficiency, reducing unburned hydrogen at the exit from 12% in the uncooled case to 7.6% in the PC40 case.

Table 1 Summary of volume average heat release in the three regions.

Heat release (MW/m^3)					
Region	Uncooled	PC40	PC23	PC10	FC22
1	16,519	25,886	21,913	21,774	22,205
2	531	2237	2225	1971	2084
3	270	880	507	361	734

In the PC23 and PC10 configurations, mass addition starts earlier at 2.3 cm and 1 cm, respectively, enhancing coolant deflagration in Region 1, as seen ahead of the detonation wave in Fig. 7(*c*). However, the lower chamber pressure leads to a 15% lower heat release than in the PC40 configuration. Two heat release streams, similar to PC40, are still observed for the PC23 case behind the oblique shock. However, the coolant deflagration occurs closer to the detonation region and the intensity of these streams reduces downstream due to the lack of coolant mass added after an axial position of 5.5 cm. This is reflected in the reduced volume-averaged heat release in Region 3 for PC23 and in both Region 2 and Region 3 for PC10. However, even with less added coolant mass, the unburnt hydrogen at the exit was measured to be 5.2 and 5% for PC23 and PC10, respectively. Suggesting that, adding coolant mass upstream is beneficial for hydrogen consumption however, with no active coolant remaining downstream, the temperatures are higher in Region 3 as seen in Fig. 4(*c*).

The heat release distribution for the FC case combines features of the PC23 and PC40 configurations. In the detonation region, heat release patterns behind and ahead of the detonation wave are similar to PC23, leading to a 35% greater heat release compared to the uncooled RDC. However, the high chamber pressure in FC22, with identical inlet conditions as other cases, reduced fuel and air mass flow by 3.2%, resulting in lower average heat release values compared to PC40. In the oblique shock region, two heat release streams, akin to those in the PC23 configuration, extend to the combustor outlet due to the higher coolant supply, which is absent in PC23. Compared to PC40, the heat release distribution for FC22 is lower in the oblique shock region because unburnt hydrogen is consumed earlier in the detonation region. Consequently, slightly lower heat release was observed in Regions 2 and 3 compared to PC40. Overall, upstream coolant injection improves hydrogen consumption. PC10 achieves the lowest unburnt hydrogen fraction at the exit (4.8%), followed by FC22 (5%), while PC40 exhibits the highest fraction (8.1%).

3.6 Circumferential Average. The overall reduction in gas temperatures due to mass addition and the overall heat release can be assessed using circumferentially averaged temperature profiles. These quantities are shown in Fig. 8 at two radial spans: 97% and 75%. Cumulative mass addition is plotted in the midrow of 97% span, and local coolant mass flow is shown in the midrow of 75% span. Each dot represents a cooling row where mass addition occurs.

In the detonation region, high chamber pressures limit the coolant mass flow from each hole to below 6 g/s. Therefore, the cooling holes in this region are not particularly effective at reducing the wall temperatures. In the film-cooled configurations, temperatures are reduced at the points of mass injection, evident as dips in the temperature profiles. So while there are some local temperatures below the uncooled case for PC23 and PC10, the average temperature up to 3 cm is nominally the same. Additionally, the increased chamber pressure alters the detonation height and modifies flow field structures, as illustrated in Fig. 2. Consequently, the temperature at 97% span in the PC40 configuration is higher than in the uncooled case.

In the oblique shock region, coolant mass flows are higher than in the detonation region and increase along the axial length as chamber pressure decreases. The higher mass flow leads to more significant temperature reduction and allows the coolant to penetrate deeper into the combustor. This is corroborated by temperature profiles at 75% span, where reductions in gas temperature are seen tracking with the coolant injection locations, similar to those at 97% span with a lower magnitude. Furthermore, temperature reductions persist at the exit, even at 75% span.

In the detonation region at 97% span, the uncooled case shows significant heat release ending at 4 cm, consistent with the height of the detonation wave. For PC40, the reduction in heat release is closer to 3 cm again tracking the reduced wave height. For this case, the heat release increased again, starting from 4 cm with the addition of coolant. The film-cooled cases cause secondary reactions that sustain heat release further downstream, as discussed in Table 1. Interestingly, the other cases do not exhibit substantial dips in heat release at the height of the detonation wave, with continuous profiles observed. In the PC10 configuration, heat release falls off at the end of its film-cooled region, around 5 cm. A similar fall off happens for the PC23 case around 8 cm. For axial regions before 4 cm, heat release at 75% span is higher compared to the uncooled case, though its magnitude is similar for all cases. Past the detonation height, the heat release levels are lower than at 97% span. This indicates that most of the coolant-driven heat release occurs closer to the outer wall.

The coolant mass flow in each row depends on the ratio of local chamber pressure to plenum pressure, with chamber plenum pressure resulting in lower local coolant mass flow. For FC22, with a chamber pressure of 1.9 bar, the coolant mass flow is lower compared to PC40, which operates at a chamber pressure of 1.75 bar, as shown in Fig. 8(*b*). Other cases also exhibit higher local mass flow relative to FC22 due to their lower chamber pressures. In the detonation region, differences in mass flow are minimal because of the high detonation pressures not allowing significant portions of the circumferential cycle to push mass flow out of the holes as discussed in Sec. 3.3.

These variations in local mass flow lead to differences in total cumulative mass flow across cases. PC10, with coolant holes located in high-pressure regions, only achieves a total mass flow of 54 g/s.

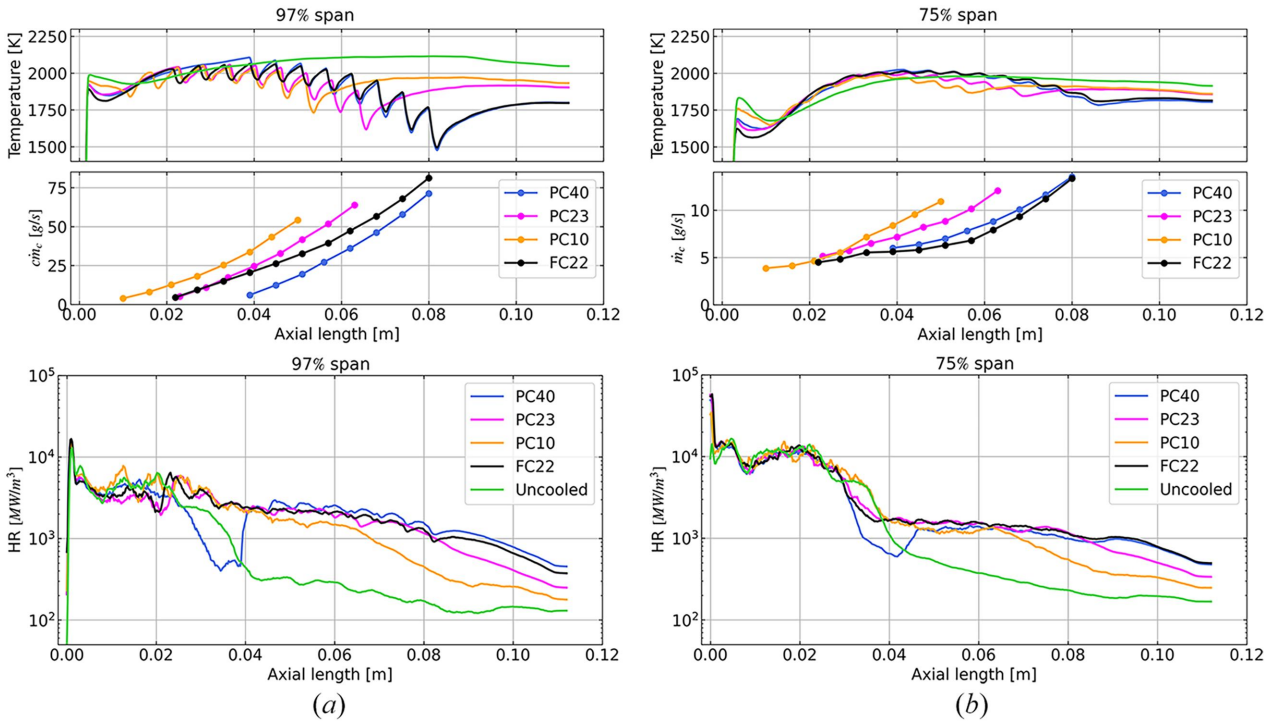

Fig. 8 The circumferentially averaged temperature is shown at the top, cumulative and local coolant mass flow in the middle, and heat release profiles at the bottom row, obtained for (*a*) 97% span and (*b*) 75% span

PC23 and FC22, which start cooling at the same location, have similar cumulative mass flow in the first three rows. However, PC23 attains higher cumulative mass flow in subsequent rows due to lower chamber pressure, resulting in a total flows of 64 g/s. Similarly, there is a downstream preference for the coolant in the FC22 configuration to exit even further downstream. This case, with its three additional downstream rows, produced a total mass flow of 81 g/s. PC40, with more cooling holes in low-pressure regions and resulted in higher local mass flow at each row then PC23 and achieved a total mass flow of 71 g/s.

In a conventional film cooling system, temperature reduction depends on local coolant mass flow and contributions from previous rows that help establish a proper film layer. This behavior is also observed in RDCs. once a particular cooling scheme has achieved a cumulative mass flow of 50 g/s, a temperature dip to approximately 1750 K is observed. Obviously, for schemes with holes further upstream, this was as cold as the outer wall could become. Beyond the final film cooling row, temperatures begin to rise due to coolant mixing with hot gases.

Overall, providing cooling further downstream has a more significant effect. In looking at the exit temperatures, the FC22 case and the PC40 case both achieve exit temperatures of approximately 1800 K. However, PC40 accomplishes this with a total coolant mass flow of 71 g/s as compared to 81 g/s for the FC22 case. This reemphasizes that the additional three upstream rows (that accounted for nominally the 10 g/s of additional coolant flow) produced small gains to the overall system cooling. In contrast, not extending the coolant as far into the oblique shock region results in far less cooling effectiveness of the outer wall. For the PC23 case, the exit temperature was still 1900 K at the exit, with an even higher temperature for the PC10 case. Remembering that each of these conditions utilized a 3 bar cooling supply, knowing where to eject the coolant is important. Trying to use this pressure to cool in the detonation region resulted in less mass flow, more hot gas ingestion, and while small gains in wall temperature were achieved locally, this was at the extent of significantly higher temperatures at the outlet.

One further consideration is that the 75% span results revealed that this coolant penetrated significantly across the width of the annulus. Since the goal of film cooling is to cool the wall and not to take away heat from the turbine, a different cooling scheme may be required. This may include using smaller angled holes, shaped holes, a different pitch spacing, or other techniques outside the scope of this investigation.

4 Conclusion

Detonation-based high power-density combustors, such as RDCs, are advantageous for gas turbine applications. However, due to their high heat release rate and harsh flow field conditions, these detonation combustors generate enormous wall thermal loads. Previous studies have suggested that film cooling could be a potential solution for managing these high heat loads.

Three partially cooled RDCs and one fully cooled RDC were compared against an uncooled combustor. The LES investigations show that adding coolant mass in an RDC is beneficial for gas turbine applications. The interaction of chamber pressure and mass addition in the detonation region influenced the mixing of fresh gases consumed by the detonation. Mass addition in the detonation region reduced the wall temperature locally. But had the further effect of significantly changing the fresh gas composition, leading to a stronger detonation wave. Additionally, coolant addition in the detonation region consumed more hydrogen, with only 4.8% unburnt hydrogen measured at the exit for PC10 compared to 8% for the PC40 case, where the coolant was injected further downstream.

However, regarding cooling performance, the holes placed in the oblique shock region provided superior cooling. The PC40 case resulted in a higher coolant mass flow for the same supply pressure, more effectively cooling the outer wall than the cases that injected coolant further upstream. The fully cooled combustor achieved comparable exit temperature reductions at PC40 but offered less effective cooling in the detonation region. The current investigations used an adiabatic wall. With thermal conduction, a more uniform wall temperature is expected, which will be lower than the average gas temperature. For the uncooled case, the average gas temperature was found to be 2000 K, while the best-performing film cooling configuration achieved a temperature reduction of 200 K.

Overall, the added coolant not only provides sufficient wall protection but also helps in consuming unburnt hydrogen through secondary reactions. These secondary reactions, however, influence the gas temperature increase near the wall. Nevertheless, when compared to the additional heat release, the benefits outweigh this effect, suggesting that film cooling is a useful tool for maintaining RDC walls below their melting temperatures.

Acknowledgment

The authors also thank Pier Carlo Nassini for his support.

Funding Data

- European Union's Horizon 2020 research and innovation program under the Marie Skłodowska-Curie "INSPIRE" (Grant Agreement No. 956803).

Data Availability Statement

The datasets generated and supporting the findings of this article are obtainable from the corresponding author upon reasonable request.

Nomenclature

FC = fully cooled combustor
GT = gas turbine
NSCBC = Navier–Stokes characteristic boundary conditions
PC = partially cooled combustor
RDC = rotating detonation combustor

Symbols

$c\dot{m}$ = cumulative mass flow (kg/s)
J = mass flux (kg/m^{2}s)
$\dot{m}$ = mass flow (kg/s)
P = static pressure (bar)
Θ = angle (degree)

Superscripts and Subscripts

c = coolant

References

[1] Lee, J. H., Ryu, J. H., Lee, E. S., Han, H. S., and Choi, J. Y., 2022, "Experimental Proof of Concept of a Noncircular Rotating Detonation Engine (RDE) for Propulsion Applications," Aerospace, **10**(1), p. 27.
[2] Fiorino, N. T., Snow, N. J., Schauer, F. R., Polanka, M. D., Schumaker, S. A., and Sell, B. C., 2022, "Improving Detonability in a Small-Scale Rotating Detonation Engine Using Partial Premixing," J. Propul. Power, **39**(2), pp. 1–10.
[3] Bach, E., Paschereit, C. O., Stathopoulos, P., and Bohon, M. D., 2020, "RDC Operation and Performance With Varying Air Injector Pressure Loss," AIAA Paper No. 2020-0199.
[4] Goto, K., Nishimura, J., Kawasaki, A., Matsuoka, K., Kasahara, J., Matsuo, A., Funaki, I., Nakata, D., Uchiumi, M., and Higashino, K., 2019, "Propulsive Performance and Heating Environment of Rotating Detonation Engine With Various Nozzles," J. Propul. Power, **35**(1), pp. 213–223.
[5] Braun, J., Sousa, J., and Paniagua, G., 2018, "Numerical Assessment of the Convective Heat Transfer in Rotating Detonation Combustors Using a Reduced-Order Model," Appl. Sci., **8**(6), p. 893.
[6] Sandri, U., Ramanagar Sridhara, S., Andreini, A., Bohon, M. D., Picchi, A., and Facchini, B., 2023, "Evaluation of Cooling Requirements for Rotating Detonation Combustors," ASME J. Turbomach., **146**(5), pp. 1–15.
[7] Ramanagar Sridhara, S., Andreini, A., Polanka, M. D., and Bohon, M. D., 2024, "LES Investigation of Film Cooling in Rotating Detonation Combustors," ASME Paper No. GT2024-123796.
[8] Tian, J., Wang, Y.-S., Zhang, J.-Z., and Tan, X.-M., 2022, "Numerical Investigation on Flow and Film Cooling Characteristics of Coolant Injection in Rotating Detonation Combustor," Aerosp. Sci. Technol., **122**, p. 107379.
[9] Yu, J., Yao, S., Li, J., Huang, Y., Guo, C., and Zhang, W., 2023, "Effects of Inlet and Secondary Flow Conditions on the Flow Field of Rotating Detonation Engines With Film Cooling," Int. J. Hydrogen Energy, **48**(24), pp. 9082–9094.

[10] Yu, J., Yao, S., Li, J., Li, J., Guo, C., and Zhang, W., 2023, "Numerical Investigation of the Rotating Detonation Engine With Cat-Ear-Shaped Film Cooling Holes Under Varying Operating Modes," Aerosp. Sci. Technol., **142**, p. 108642.
[11] Chriss, S. L., 2022, "Characterization of a Rotating Detonation Engine With an Air Film Cooled Outer Body," Ph.D. thesis, University of Dayton, Dayton, OH.
[12] Yu, J., Yao, S., Li, J., Li, J., Lei, Y., Wang, R., and Zhang, W., 2024, "Experimental Investigation of the Hydrogen-Air Rotating Detonation Engine With Cat-Ear-Shaped Film Cooling Holes," Int. J. Hydrogen Energy, **89**, pp. 1454–1465.
[13] Bach, E., Paschereit, C. O., Stathopoulos, P., and Bohon, M. D., 2021, "An Empirical Model for Stagnation Pressure Gain in Rotating Detonation Combustors," Proc. Combust. Inst., **38**(3), pp. 3807–3814.
[14] Bluemner, R., Gutmark, E. J., Paschereit, C. O., and Bohon, M. D., 2021, "Stabilization Mechanisms of Longitudinal Pulsations in Rotating Detonation Combustors," Proc. Combust. Inst., **38**(3), pp. 3797–3806.
[15] Bach, E., Bohon, M. D., Paschereit, C. O., Berlin, T. U., and Dynamics, F., 2018, "Development of an Instrumented Guide Vane Set for RDC Exhaust Flow Characterization," AIAA Paper No. 2018-4479.
[16] Bach, E., Stathopoulos, P., Paschereit, C. O., and Bohon, M. D., 2020, "Performance Analysis of a Rotating Detonation Combustor Based on Stagnation Pressure Measurements," Combust. Flame, **217**, pp. 21–36.
[17] Ramanagar, S., Andreini, A., Polanka, M. D., and Bohon, M. D., 2024, "The Impact of Film Cooling on the Heat Release Within a Rotating Detonation Combustor," Appl. Energy Combust. Sci., **20**, p. 100300.
[18] Schonfeld, T., and Rudgyard, M., 1999, "Steady and Unsteady Flow Simulations Using the Hybrid Flow Solver AVBP," AIAA J., **37**(11), pp. 1378–1385.
[19] Gicquel, L. Y., Gourdain, N., Boussuge, J.-F., Deniau, H., Staffelbach, G., Wolf, P., and Poinsot, T., 2011, "High Performance Parallel Computing of Flows in Complex Geometries," C. R. Méc., **339**(2–3), pp. 104–124.
[20] Gicquel, L., Staffelbach, G., and Poinsot, T., 2012, "Large Eddy Simulations of Gaseous Flames in Gas Turbine Combustion Chambers," Prog. Energy Combust. Sci., **38**(6), pp. 782–817.
[21] Barré, D., Kraushaar, M., Staffelbach, G., Moureau, V., and Gicquel, L. Y., 2013, "Compressible and Low Mach Number LES of a Swirl Experimental Burner," C. R. Méc., **341**(1–2), pp. 277–287.
[22] Nassini, P. C., Andreini, A., and Bohon, M. D., 2023, "Characterization of Refill Region and Mixing State Immediately Ahead of a Hydrogen-Air Rotating Detonation Using LES," Combust. Flame, **258**, p. 113050.
[23] Celik, I. B., Cehreli, Z. N., and Yavuz, I., 2005, "Index of Resolution Quality for Large Eddy Simulations," ASME J. Fluids Eng., Trans. ASME, **127**(5), pp. 949–958.
[24] Zhao, N., Meng, Q., Zheng, H., Li, Z., and Deng, F., 2020, "Numerical Study of the Influence of Annular Width on the Rotating Detonation Wave in a Non-Premixed Combustor," Aerosp. Sci. Technol., **100**, p. 105825.
[25] Shen, D., Cheng, M., Rong, G., Sheng, Z., Zhang, Y., and Wang, J., 2024, "Effects of Film Cooling Injection Inclination Angle on Cooling Performance in Rotating Detonation Combustors," Phys. Fluids, **36**(2), p. 026118.